LAWRENCE
LIVERMORE
NATIONAL
LABORATORY

UCRL-JRNL-224783

# Enhancement of T1 and T2 relaxation by paramagnetic silica-coated nanocrystals

Daniele Gerion, Julie Herberg, Erica Gjersing, Erick Ramon, Robert Maxwell, Joe W. Gray, Thomas F. Budinger, Fanqing Frank Chen

September 27, 2006

Journal of Physical Chemistry C

# Enhancement of $T_1$ and $T_2$ relaxation by paramagnetic silica-coated nanocrystals

Daniele Gerion,[1,*] Julie Herberg, [1] Erica Gjersing, [1] Erick Ramon[1]
Robert Maxwell[1], Joe W. Gray[2], Thomas F. Budinger[2], Fanqing Frank Chen[2]

[1] *Lawrence Livermore National Laboratory, Livermore, CA, 94551;*
[2]*Lawrence Berkeley National Laboratory, Berkeley, CA 94720*

We present the first comprehensive investigation on water-soluble nanoparticles embedded into a paramagnetic shell and determine their properties as an MRI contrast agent. The nanoprobes are constructed with an inorganic core embedded into an ultra-thin silica shell covalently linked to chelated Gd(III) ions. The chelator consists in the molecule DOTA and the inorganic cores are fluorescent CdSe/ZnS qdots or Au nanoparticles. Optical properties of the cores (fluorescence emission or plasmon position) are not affected by the neither the silica shell nor the presence of the chelated paramagnetic ions. The resulting complex has a diameter of 8 to 15 nm and is soluble in high ionic strength buffers at pH ranging from ~4 to 11, even at concentrations exceeding 50 μM. In MRI experiments at clinical field strengths of 60 MHz, the MRI nanoprobes posses spin-lattice ($T_1$) and a spin-spin ($T_2$) relaxivities of ~1000 $mM^{-1}s^{-1}$ and 2500 $mM^{-1}$ $s^{-1}$ respectively for probes having ~ 8 nm and about 16000 $mM^{-1}s^{-1}$ for 15 nm probes. The relaxivity has been correlated to the number of Gd(III) covalently linked to the silica shell. At 60 MHz, each bound chelated Gd(III) contributes by over 23 $mM^{-1}s^{-1}$ to the total $T_1$ and by over 54 $mM^{-1}s^{-1}$ to the total $T_2$ relaxivity respectively. The sensitivity of our probes is in the 100 nM range for 8-10 nm particles and reaches 10 nM for particles with approximately 15-18 nm in diameter, and can be improved by packing more Gd(III) on the surface. Preliminary dynamic contrast enhancement MRI experiments in mice reveal that silica-coated MRI probes are cleared from the renal system into the bladder within minutes, with no observable effects on the health of the animal. In vivo biocompatibility and the ease of further functionalization should expand the range of applications beyond angiogenesis.

* To whom correspondence should be addressed: danielegerion@yahoo.com

Recent years have witnessed a new age in fluorescence imaging driven by remarkable advances in detection technologies. The ability to discern fluorescent markers at the single molecule level is important for molecular imaging, in particular for monitoring signaling pathways in live cells or for the study of cellular metabolism.[1] Qdots represent a new form of fluorescent agents that possess many of the properties to perform these studies.[2] They have the size of a protein and can be programmed to acquire biological functions, they are well tolerated by live cells, they afford multiplexed detection due to their tunable emission, they are resistant to photobleaching, and they can be tracked at the single molecule level over extended periods of time. [3, 4] Thus, by using biologically engineered QDs, there is great potential for learning more about the molecular basis of certain diseases, such as cancer, and finding a therapeutic treatment. [5, 6]

For this noble cause, a big leap forward has to be taken to correlate the deficiency of a cell *in vitro* to a disease *in vivo*. Cells reside in highly structured 3D environments. They are sensitive to the extracellular matrix and to the presence of neighboring cells with which they make mechanical or biochemical contact. Although most diseases originate from the malfunction of a single cell, whether the disease spreads ultimately depends on whether the cell and its daughters can survive and proliferate by beating the feedback control mechanisms in a complex 3D multicellular organism. It is therefore important to know not only what happens within a single cell but also how cells communicate and socialize and how they respond to stimuli *in vivo*.

In this regard, the use of bioengineered QDs is problematic because fluorescence has one notorious shortcoming: light has a penetration depth of less than a few millimeters in the best case. As a result, fluorescence is a powerful tool mainly limited to *in vitro* imaging. *In vivo* medical applications, such as detection of tumors or metastatses, or the tracking of stem cells after cell therapy treatment require a different set of non-invasive imaging probes and techniques.[7-9]

Magnetic resonance imaging is a method of choice for *in vivo* visualization because of its infinite penetration depth and its anatomic resolution. MRI has the ability to map the relaxation processes of water protons in the sample, referred as $T_1$ and $T_2$ relaxation times. One of the powers of MRI is its ability to extract image contrast, or a difference in image intensity between tissues, on the basis of variations in the local proton environment. Unfortunately, intrinsic differences between tissues are often too small to provide distinguishable relaxation times for protons, and the resulting contrast between tissues is

often too weak for a firm diagnosis. This is why exogenous contrast agents are often used, most notably in the form of small amounts of paramagnetic impurities, such as chelated Gd(III),[10] linked to a targeting biomolecule.[11] They accelerate the $T_1$ and $T_2$ relaxation processes of water protons in their surrounding. However, even in such case, the contrast obtained in MRI might not be strong enough, because the contrast agent by itself does not provide enough sensitivity. Considerable efforts have focused in developing contrast agents with improved properties.

The performance of a contrast agent in solution is measured by its relaxivity, defined as $1/T_i \sim r_i *[C]$, *i=1,2*, where $r_i$ is the relaxivity and [C] the concentration of the contrast agent. The rule is that higher its relaxivity, the more sensitive the contrast agent. $T_1$-contrast agents are agents that affect mostly the longitudinal relaxation time. They are usually made of chelated lanthanide ions and reach relaxivities of 5-50 $mM^{-1}s^{-1}$. [12] Higher relaxivities are obtained with $T_2$-contrast agents, i.e. agents that affect mainly the transversal relaxation time, which is the most prominent of which are iron oxide nanoparticles. These particles, used in clinical trials, have sizes around 50-200 nm in diameter. At this size range, they often exhibit a hysteresis curve upon application of a reversal magnetic field, a sign that the magnetic moment is tightly bound to the crystal structure. Superparamagnetic behavior (i.e. no hysteresis upon a switching field) is preferred for MRI applications. The SP regime is the realm of smaller magnetic nanoparticles with core sizes below ~20 nm, often labeled SPIO (Small Superparamagnetic Iron Oxide). [13] Decreasing the size of the SPIO nanoparticles also leads to a decrease in their total magnetic moment and reduces their contrast power. In this work, we present and characterize a probe construct that reaches $T_1$ and $T_2$ relaxivities of up to approximately 13'000 and ~15'000 $mM^{-1}s^{-1}$ at clinical fields while its size is only 15-18 nm. Smaller constructs of size in the range of 8-10 nm exhibit relaxivities of approximately 1000 and 2500 $mM^{-1}$ $s^{-1}$.

The construct consists in an inorganic nanoparticle core (fluorescent CdSe/ZnS or Au) embedded into a thin paramagnetic silica shell. These silica-coated scaffolds are about 10 nm in size and are used to covalently anchor multiple GdDOTA molecules. We present evidence that a multi-component mechanism contributes to these exceedingly high relaxivity values. The mechanism involves a large number of GdDOTA moieties, the slowing of tumbling rate of GdDOTA and the hydrophilicity of the silica surface. In fact, the number of GdDOTA moieties linked to the silica shell can be tuned from 20 up to 320 and in some cases above a few thousend, and each unit contributes additively to the total relaxivity. Moreover, we observe that the $T_1$ and $T_2$ relaxivities per GdDOTA unit (or ion relaxivity) is increased by a factor of 5 and 10 respectively when GdDOTA is bound to the silica shell compared to its mobile form in solution, and by a factor of 2 and 3 respectively compared to the case when GdDOTA is linked to nanoparticles through a flexible, weakly hydrophilic phospholipids layer.

The design of our probe can be easily extended to cover PET imaging, and we do not foresee any difficulty to enhance the capability of the silica-coated probes by adding a targeting mechanism. We will discuss a set of advantages provided by paramagnetic silica shells over polymeric coatings.

## 2 Experimental Details

### 2.1 Synthesis and characterization of silanized CdSe/ZnS QDs and Au nanocrystals coated with Gd-DOTA

In both cases, we use a three-steps process: first we grow a PEG-ylated silica shell containing thiol groups around the inorganic cores (semiconductor or metalic); second we synthesize paramagnetic agents made of an amine-terminated DOTA molecules that chelates Gd(III) ions; third we covalently crosslink the chelated paramagnetic compound to silanized particles using a bifunctional cross-linker.

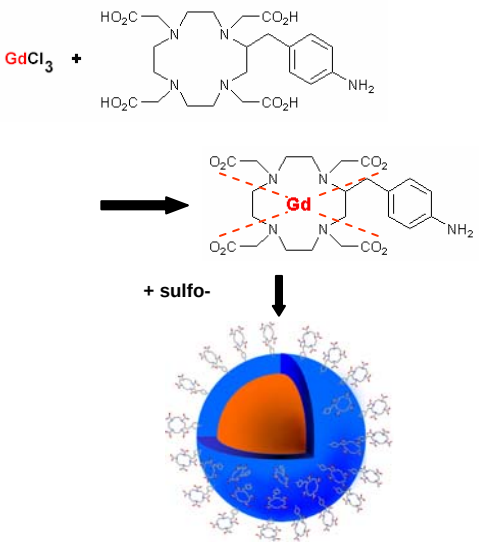


**Scheme 1:** Scheme for the preparation of the paramagnetic probes. Gadolinium chloride is reacted with a DOTA complex under controlled acidic conditions at 80ºC. Gd(III) is stabilized inside DOTA by hydrogen bonds with the carboxylic groups (dash line). Subsequently, the amine group, which does not take part in Gd(III) complexion, is converted into a maleimide group which will react with thiols on the silica-coated nanoparticles. The payload of GdDOTA per nanoparticles depends on the surface area. It can vary from ~50 up to several hundreds. Due to this coupling scheme, Gd(III) is stably chelated in PBS buffer over periods exceeding a few months.

**Silanization of QDs:** The synthesis and silanization of CdSe/ZnS QDs, or simply $SiO_2$@QD, follow published procedures.[14, 15] Briefly, after a priming step replacing TOPO surfactants on the QD surface with MercaptoPropyltrimethoxySilane (MPS), polymerization of siloxane is performed in methanol under slightly basic conditions. In a second step, addition of fresh MPS and PEG-propyltrimethoxysilane permits the introduction of functional (SH) and stabilizing (PEG) groups respectively into the forming $SiO_2$ shell. Silane polymerization is quenched with trimethylchlorosilane that converts reactive silanol groups into methyl groups. This allows controlling and limiting the size of the silica shell to a thickness of a few nanometers. After extensive dialysis against fresh methanol and subsequently against 10 mM phosphate buffer, pH~7-7.5, silanized QD solutions are concentrated using centricon 100 down to optical densities greater than 30-70 and purified further by low pressure chromatography using a 20 cm long, 1cm ID column filled with sephadex G200 or sephadex G100. Silanized qdots elute in a rather large band. Typically, we load approximately 500-700 µl of solution and collect ~ 5 ml of solution. Solutions of silanized Qdots are stored at room temperature at optical densities in the range of 3-6.

**Silanization of Au nanoparticles:** A similar approach is used to silanize citrate- stabilized Au nanoparticles of 5 nm and 10 nm purchased at BBI International. However, in the case of colloidal Au, silanization is performed in an aqueous environment because the particles would not disperse in methanol. Since citrate-coated Au nanoparticles aggregate easily even in low ionic strength buffers, the Au colloids are first stabilized with a phosphine surfactant, as we have reported previously [16, 17]. Phosphine-stabilized Au colloids are precipitated with ethanol and resuspended into a solution of 1:1000 v:v MPS in water to exchange the capping ligands to a thiolated siloxane. After this priming step, an approach similar to the QDs case is taken, with the growth of a shell using MPS and PEG-silane, quenching of the shell growth using trimethylchlorosilane. All these steps are however performed in water. After the procedure is completed, silanized Au colloids are purified using centrifugation. Silica-coated Au nanocrystals can be concentrated with a centricon 100 device to dryness. Upon addition of buffer, the particles resuspend spontaneously by a gentle shake. Such purification is performed several times. Despite these multiple washing steps and large concentrations (optical densities in the range >100), the plasmon peak of silanized Au colloids measured by UV-Vis does not shift compared to the original diluted samples for both 5 and 10 nm colloids. We take it as a sign that silanization did not induce aggregation of the particles.

The size estimates of the silanized particles are based on previous AFM investigations because the thin silica shell is hardly visible under a TEM. Based on those studies, our estimate is that the silica shell is about 2-3 nm thick and adds 4-6 nm to the particle diameter. In this study, we focus on ~5 nm naked CdSe/ZnS, and 5 nm and 10 nm citrate-stabilized Au colloids. After silanization, the respective sizes are ~10 nm for silanized QDs, ~10 nm for 5-nm Au, and ~16-18 nm for 10 nm Au.

**Gd(III) chelation with a DOTA moiety:** The synthesis of GdDOTA, *i.e.* one Gd(III) ion chelated by DOTA, is performed according to the procedure, adapted from previous reports. [18, 19] We dissolve p-$NH_2$-Bn-DOTA, *i.e.* 2-(4-Aminobenzyl)-1,4,7,10-tetraazacyclododecane-1,4,7,10-tetraacetic acid, (Macrocyclics Inc., hereafter called simply DOTA) in water and add an aqueous solution of $GdCl_3$ (Sigma-Alrich), so as to have a 1: .98 molar mixture of DOTA:Gd(III) and ~0.2 M concentration in DOTA. The solution is heated a few seconds to 80°C to favor complexion of Gd(III) with the tetraazacyclododecane ring. The pH of the solution drops below 1. We bring the pH to 3.5-4 by adding aliquots of 7M NaOH and heat the solution back to 80°C for a few minutes. At this early stage, heating produces acidification of the solution. Therefore, we repeated heating-adjusting the pH to 3.5-4 with sodium hydroxide several times (up to 7 times) until the heating step does not produce a drop in pH below 3.5. At that stage, the solution is kept at 80°C for 3 hrs. Completion of the Gd(III) chelation is confirmed by a colorimetric assay using Arsenazo dye (Sigma-Alrich). This colorimetric dye reacts to the presence of unbound Gd(III). The dye natural color is purple, but upon complexion with Gd(III), its color turns to blue. After 3 hrs, the GdDOTA solution is slightly yellowish and has a concentration of approximately 150 mM in GdDOTA, deduced from the initial amount of DOTA, $GdCl_3$ and NaOH used. The stability of the GdDOTA has been studied only summarily using the colorimetric Arsenazo test. No Gd(III) release from the DOTA ring was observed over a period of several weeks.

**Linking GdDOTA to silanized nanoparticles:** Freshly prepared paramagnetic GdDOTA is covalently linked to silanized nanoparticles to form GdDOTA-$SiO_2$@Particle. First the amino group on the GdDOTA unit is converted into a maleimide group using sulfo-SMCC and classic bioconjugation conditions (pH ~ 6-6.5, SMCC:DOTA ~ 3:1). [20] After one hour reaction, the maleimide-activated GdDOTA is directly reacted to silanized particles. The reaction is kept running for ~24 hrs at room temperature. Removal of unbound GdDOTA is performed by a 48 hrs dialysis in a 50K MWCO membrane (SpectraPor 6) against a bath consisting in 10 mM phosphate buffer, pH ~ 7. We exchange the buffer bath at least 4 times during the dialysis period. After dialysis, the sample is further purified by 4 to 5 runs of centricon 100. For each run, 2 ml of silanized particles are condensed down to <100 µl and ~ 1.9 ml of fresh buffer is added. After these extensive purification steps, we estimate that the concentration of

unbound GdDOTA is in the fM-pM range, far too small to provide any signal in MRI and far smaller than a few μMs, the typical concentration of silanized nanoparticles.

**Determination of the concentration of the samples:** The concentrations of our solutions are given in terms of silanized nanoparticle concentration and not in terms of Gd(III) present in solution. This seems to be a wise choice, if one considers that all Gd(III) are concentrated onto the nanoparticle surface and the solution is not homogenous in Gd(III). [at 1 μM concentration, the average distance between nanoparticles is ~ over 100 nm; there is no unbound Gd(III) in the space between nanoparticles, this latter being highly localized onto the nanoparticles].

We measure the UV-Vis spectrum and deduce the concentration of the solution from the optical density at the exiton (for semiconductors – QDs) or plasmon (for Au colloids) peak using known extinction coefficients and the following equation: $C = OD / (\varepsilon \cdot \delta)$, where OD is the optical density or amplitude of absorption at the exiton/plasmon peak, δ is the cuvette length (usually 1 cm or 2 mm) and ε is the extinction coefficient. The extinction coefficients are deduced from the literature (QDs) or given from the manufacturer (Au). We use the following numbers: QD exiton peak at ~ 610 nm, fluorescence emission at ~ 630 nm, fwhm ~38 nm, extinction coefficient used 620'000 $M^{-1}cm^{-1}$ following published reports. [21] For 5 nm an 10 nM Au colloid, both plasmon peaks are at 524 nm and we use $\varepsilon = 1{,}2 \times 10^7\ M^{-1}cm^{-1}$ for 5 nm Au and $\varepsilon = 1.06 \times 10^8\ M^{-1}cm^{-1}$ for 10 nm Au respectively. These later numbers are computed from the concentrations given by the manufacturer and the OD of citrate-stabilized Au colloids measured directly out of the bottle.

**Determination of the number of Gd per silanized nanoparticle:** After extensive purification from unbound GdDOTA, these samples are chemically analyzed by ICP-MS by measuring the total amount of Gd and Cd or Au ions. By assuming bulk parameters of the CdSe or Au lattice and the size of the nanoparticles (using tabulated values linking the size of the QDs to its optical properties, or the claimed size for Au nanocrystals), we deduce the number of Gd per silanized nanoparticle. The same samples were previousely analyzed by MRI. The number of GdDOTA per GdDOTA-$SiO_2$@Particle varies from ~3 to >300 and depends on the size of the initial nanoparticles and the conditions used during bioconjugation.

### 2.2 20 MHz and 60 MHz NMR Minispec Parameters

$T_1$ and $T_2$ relaxation time measurements were performed on a Bruker Minispecs operating at 20MHz and 60MHz. An inversion recovery pulse sequence was employed for $T_1$ relaxation time measurements using a mono exponential fit to the recovery curve. For each experiment 4 scans were collected with a recycle delay of 15 seconds. To obtain the recovery curve, 50 evenly spaced points were collected with the first point acquired at 5 ms. The last time point was collected at 4000 ms for short $T_1$ samples and 10,000 ms for samples with long $T_1$ so that each sample was allowed to fully recover. The receiver gain for each sample was set so that the signal amplitude was approximately 60%.

$T_2$ times were calculated from a mono exponential fit to a spin echo decay curve using a CPMG pulse sequence. Eight scans were acquired for each experiment with an echo time of 1ms, pulse attenuation of 6dB, and recycle delay of 3 seconds. The number of echo times was varied between 100 points, for short $T_2$s, and 3500 points, for long $T_2$s, in order to 1acquire the full decay curve for each sample. The receiver gain for each sample was set to the same value that was used in the $T_1$ experiment.

### 2.3 Bruker 2.5mm MicroImaging MRI system parameters

All MRI experiments were performed on a Bruker Avance 400 MHz spectrometer equipped with a high-resolution Micro5 microimaging system with a 25 mm rf coil. To obtain spin-lattice relaxation ($T_1$) values, a Fast Imaging with Steady State Precession (FISP) with Inversion Recovery (IR) Sequence was used. The MRI parameters for FISP include echo time of 1.5 ms, repetition rate of 3.0ms, 8 averages, number of segments of 32, field-of-view of 3x3 cm, resolution of 234x234, microns/pixel, flip angle (alpha) of 60°, and inversion delay ($T_1$) of 235.5 μsec. To obtain spin-spin relaxation ($T_2$) times a Multi Slice Multi Echo (MSME) Sequence was employed. The MRI parameter for MSME including number of echoes of 32, time of echo is 13.8 ms, repetition rate of 10,000 ms, field-of-view of 3x3 cm, resolution of 117x117 microns/pixel, number of averages = 1, and slice thickness = 1 mm.

### 2.3 Mice imaging using a GE 1.5T MRI system

## 3. Results

To determine if nanoparticles embedded into a silica shell and linked to chelated paramagnetic ions are sensitive contrast agents for MRI, we first present the case of paramagnetic silanized semiconductor QDs samples, with QD core size of ~ 5nm. Subsequently, we will show that paramagnetic silanized metallic Au nanoparticles exhibit similar results. Comparison of MRI data obtained for GdDOTA-$SiO_2$@P, where P represents nanoparticles of different nature and sizes will shed light on the nature of the mechanism of contrast enhancement.

First, images were collected of 4 μM GdDOTA-$SiO_2$@QD and compared to control solutions. Control

samples include: a) 4 μM $SiO_2$@QD; b) 4 μM DOTA-$SiO_2$@QD lacking the activation with Gd(III); c) 10 mM phosphate buffer, pH ~ 7, the common buffer for these solutions. In the same set of experiments, unbound GdDOTA at concentrations ranging from 390 μM to 7350 μM is also profiled. This latter is a clinically approved contrast agent, better known under the trademark DOTAREM® and $T_1$ and $T_2$ measurements produced similar results to previously reported data.[23] Simultaneous data acquisition permits a direct comparison of the performance of current contrast agents with our paramagnetic silica-coated nanoprobes.

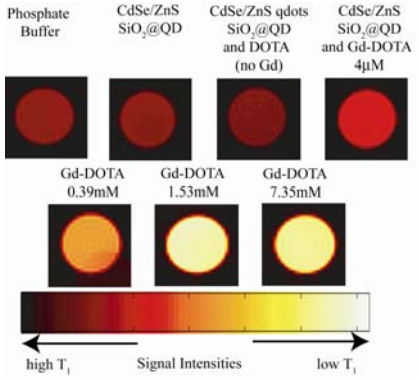


**Figure 1** The spin-lattice relaxation MRI images ($T_1$ weighted images) taken using a Fast Imaging with Steady State Procession (FISP) with inversion recovery (IR) sequence of PBS buffer, $SiO_2$@QD, DOTA-$SiO_2$@QD lacking the paramagnetic load and GdDOTA-$SiO_2$@QD, at 400MHz and room temperature. Only the paramagnetic silica-coated nanoparticles exhibit a contrast.

Figure 1 shows the spin-lattice relaxation MRI images ($T_1$ weighted images). Although qualitative differences in the MRI images clearly establish that only paramagnetic GdDOTA-$SiO_2$@QD provide a marked contrast, a clearer picture emerges from quantitative evaluation of the longitudinal relaxation times $T_1$, by plotting $M/M_o$ verses log(τ(ms)), i.e. the residual magnetization as a function of the recovery time. $T_1$ are measured by fitting $M(\tau)/M_o$ to an single exponential growth curve: $(M(\tau)/M_o)= (1-\exp(\tau/T_1))$. $T_1$ recovery curves are not shown; however the values are summarized in Table 1. The GdDOTA-$SiO_2$@QD sample with a QD concentration of 4μM has a $T_1$ of 186ms, significantly lower than the longitudinal relaxation times of control QD solutions where $T_1$ was about 600 ms, or from buffer solutions with $T_1 \sim 420$ ms. The presence of chelated Gd(III) linked to the silica shell produces a 3-fold decrease in $T_1$.

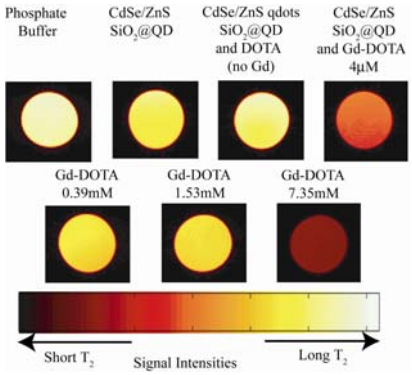


**Figure 2:** A spin-spin relaxation MRI images ($T_2$ weighted images) were taken using a Multi Slice Multi Echo (MSME) sequence of PBS buffer, $SiO_2$@QD, DOTA-$SiO_2$@QD lacking the paramagnetic load and GdDOTA-$SiO_2$@QD, at 400MHz and room temperature. Notice the stronger effect of GdDOTA-$SiO_2$@QD on $T_2$ rather than $T_1$.

| Sample name | $T_1$ [ms] | $T_2$ [ms] |
|---|---|---|
| PBS buffer | 414 | 425 |
| $SiO_2$@QD | 600 | 345 |
| DOTA-$SiO_2$@QD | 577 | 347 |
| GdDOTA-$SiO_2$@QD | 186 | 77 |
| GdDOTA, 390 mM | 237 | 201 |
| GdDOTA, 1530 mM | 147 | 123 |
| GdDOTA, 7350 mM | 59 | 37 |

**Table 1:** $T_1$ and $T_2$ values of PBS buffer, $SiO_2$@QD, DOTA-$SiO_2$@QD lacking the paramagnetic load and GdDOTA-$SiO_2$@QD, and various concentrations of GdDOTA from 0.39mM to 7.35mM at 400MHz and at room temperature.

A similar approach is used to measure the transversal relaxation time $T_2$ of the same samples. Spin-spin relaxation MRI images ($T_2$ weighted images) were taken using a Multi Slice Multi Echo (MSME) sequence and are shown in Fig.2. Transversal relaxation times were determined by a plot of log $(M/M_o)$ verses τ(ms). The $T_2$ times were computing by fitting $\log(M/M_o)$ to a linear decay curve of log $(M/M_o) = \tau/T_2$. The $T_2$ recovery curves are not shown; however the values are summarized in Table 1. The transversal relaxation time of 4 μM GdDOTA-$SiO_2$@QD is ~77 ms, much shorter than the $T_2$ of all other control samples where $T_2$ is in the 345 ms to 425 ms range. In this case, the presence of chelated Gd(III) linked to the silica surface produces a 4-fold decrease in $T_2$ compared to control solutions. As it is clear from Fig. 1, GdDOTA-$SiO_2$@QD solutions have a stronger influence on the transversal relaxation time than on the longitudinal one.

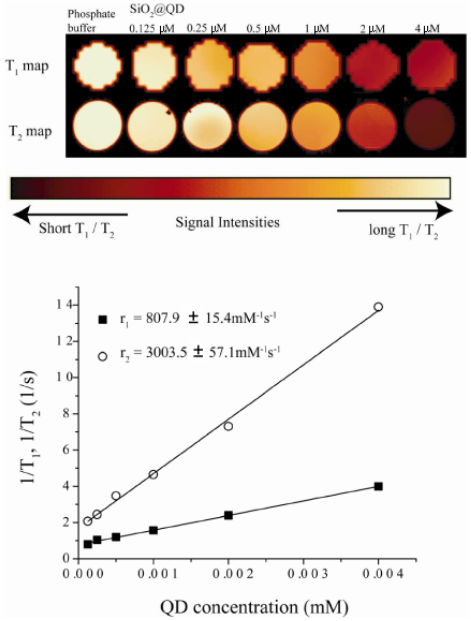


**Figure 3: a)** $T_1$ and $T_2$ MRI maps taken at various concentrations of GdDOTA-$SiO_2$@QD ranging from 0.125 µM to 4 µM at 400 MHz and at room temperature. During the same experiment, Gd-DOTA at a Gd(III) concentration of 390 µM and a phosphate buffer have also been imaged as a reference controls. **b)** Plots of $1/T_1$ and $1/T_2$ verses nanoparticle concentration are shown for the same samples. The slopes represent the relaxivity and correspond to $r_1$=807.9 ± 15.4 $mM^{-1}s^{-1}$ and $r_2$=3003.5 ± 57.1 $mM^{-1}s^{-1}$. Ion relaxivities, i.e. relaxivity per Gd ion, are $r_1$=17.9 ± 0.34$mM^{-1}s^{-1}$ and $r_2$=67 ± 1 $mM^{-1}s^{-1}$.

It is worth noticing that only paramagnetic GdDOTA-$SiO_2$@QD provide a contrast in MR Images. All solutions lacking the paramagnetic load exhibit MRI images and relaxation times that barely depart from the buffer environment. Moreover, $T_1$ and $T_2$ values of 4 µM GdDOTA-$SiO_2$@QD solutions are similar to relaxation values measured for unbound GdDOTA with a Gd(III) concentration of approximately 800-2500 µM.[22] It may be tempting to conclude that there are about 200-600 GdDOTA per $SiO_2$@QD, however such extrapolation will prove to be incorrect as we will discuss later. Similar qualitative results were observed for GdDOTA-$SiO_2$@Au, with nanocrystal cores of 5 and 10 nm diameter. MRI measurements presented so far indicate that GdDOTA-$SiO_2$@QD with a nanoparticle concentration in the µM range has the same contrast power than GdDOTA with Gd(III) concentration in mM range.

To quantify this increase in sensitivity, MRI measurements were taken at various concentrations of contrast agent, and relaxivities were computed. GdDOTA-$SiO_2$@QD with nanoparticle concentration ranging from 0.125µM to 4µM and unbound GdDOTA with Gd(III) concentration of 390 µM to 7150 µM were investigated simultaneously. The $T_1$ and $T_2$ maps are shown in Figure 3a. In the lower panels, we show the linear behaviors of the inverse relaxation times versus the contrast agent concentrations, $1/T_i \sim r_i$* C, i=1,2. The slopes $r_i$ represent the relaxivity of GdDOTA-$SiO_2$@QD (GdDOTA, values in brackets) and correspond to $r_1$=807.9 ± 15.4 (3.66 ± 0.04) $mM^{-1}s^{-1}$ and $r_2$=3003.5 ± 57.1 (3.8 ± 0.2) $mM^{-1}s^{-1}$ at 400 MHz.

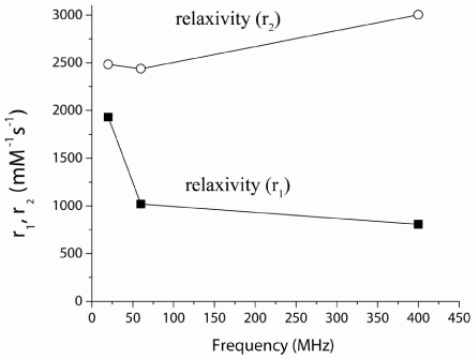


**Figure 4.** Relaxivities of GdDOTA-$SiO_2$@QD as a function of the proton Larmor frequency. The lines are guides for the eyes. The trend is similar to that of unbound GdDOTA. Notice however how the $T_2$ relaxivity is always larger than the longitudinal one.

| Frequency [MHz] | $R_1$ relaxivity [$mM^{-1}$ $s^{-1}$] | $R_2$ relaxivity [$mM^{-1}$ $s^{-1}$] |
|---|---|---|
| 20 | 1932.0 ± 36.7 (42.9 ± 0.8) | 2483.6 ± 47.2 (55.2 ± 1.1) |
| 60 | 1018.6 ± 19.4 (22.6 ± 0.4) | 2438.1 ± 46.3 (54.2 ± 1.0) |
| 400 | 807.9 ± 15.4 (17.9 ± 0.3) | 3003.5 ± 51.7 (66.7 ± 1.3) |
| GdDOTA 20-100 | 3-5 | 3-5 |

**Table 2:** Relaxivity values at different fields measured at room temperature. In parenthesis is the value of the Gd(III) ion relaxivity. This is deduced from the measurement of Gd concentration per nanoparticles with ICP-MS. The bottom line serves as comparison with the Gd(III) ion relaxivity of unbound GdDOTA.

So far, we have focused on the capability of GdDOTA-$SiO_2$@QD to deliver a contrast signal using a 400 MHz imaging system. However, most clinical scanners operate at 60 MHz. To investigate the behavior of our probes at 20 MHz and 60 MHz, we used a Bruker NMR Minispec. The instrument does not afford imaging but allows the measurement of $T_1$ and $T_2$ from which relaxivities are deduced as described above. The longitudinal relaxivity $r_1$ at 20 MHz and 60 MHz was determined to be $r_1$=1932.0 ± 36.7 $mM^{-1}s^{-1}$ and $r_1$=1018.6 ± 19.4$mM^{-1}s^{-1}$ respectively. The transversal relaxivity $r_2$ for 20 MHz and 60 MHz was $r_2$=2483.6 ± 47.2 $mM^{-1}s^{-1}$

and $r_2$=2438.1 ± 46.3 $mM^{-1}s^{-1}$. Relaxivities are summarized in Table 2 and in Fig. 4. Although we only have three data points, they seem to qualitatively follow the Nuclear Magnetic Relaxation Dispersion (NMRD) profile observed for unbound GdDOTA. [23, 24] In particular, $r_1$ is strongly field-dependent. It decreases from ~2000 $mM^{-1}s^{-1}$ at 20 MHz to ~ 800 $mM^{-1}s^{-1}$ at 400 MHz. $r_2$, as expected, exhibits a very slight increase with increasing fields. Notice how, at all frequencies, the transversal relaxivity of GdDOTA-$SiO_2$@QD is larger than the longitudinal one. Therefore, GdDOTA-$SiO_2$@QD appears to be a $T_2$ contrast agent, even tough unbound GdDOTA affects mainly the longitudinal relaxation time.

At the three field strengths investigated here, the relaxivities of GdDOTA-$SiO_2$@QD reach values over 800-3000 $mM^{-1}s^{-1}$, while the relaxivities of unbound GdDOTA ceils at 3-12 $mM^{-1}s^{-1}$. We determined by ICP-MS that there are approximately 45 chelated Gd ions per $SiO_2$@QD in the samples presented above. Consequently, at 60 MHz for instance, every GdDOTA of the GdDOTA-$SiO_2$@QD probe contributes for about 22.6 ± 0.4 $mM^{-1}s^{-1}$ to $r_1$ and 54.2 ± 0.3$mM^{-1}s^{-1}$ to $r_2$. This represents a six-fold increase for $r_1$ and twelve-fold increase for $r_2$ compared to the value found for unbound GdDOTA at the same field strength.

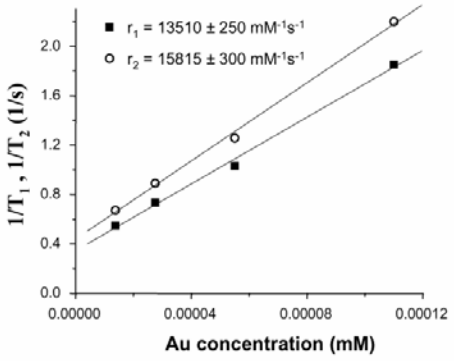


**Figure 5** Relaxivity of 10 nm Au colloids coated with a paramagnetic silica shell at 20 MHz. The total size of the particles (including the silica shell) is about 15-18 nm . The particles contain more than 300 GdDOTA, thereby reaching relaxivity values close to those of organic dendrimers of generation N=7.

To explore the cause of the increase in ion relaxivity, we initially speculated that the permanent electric dipole of QDs [25] may affect the local environment that chelated Gd experience through a dipole coupling. This ultimately perturbs the dynamics of water molecules in their neighborhoods. To test our assumption, QD nanoparticles were replaced with dipole-free cores such as gold. Thus, we developed the silanization of colloidal gold nanoparticles with 5 nm and 10 nm diameter (Fig.5). The smaller Au nanoparticles have the same size than CdSe/ZnS QD cores. At 20 MHz, we measured $r_1$ = 2165.8 ± 41.2 $mM^{-1}s^{-1}$ and $r_2$= 2709.9 ± 51.5 $mM^{-1}s^{-1}$ for silanized 5 nm Au colloids with about 60 GdDOTA (determined by ICP-MS). For silanized 10-nm Au with over 320 GdDOTA, we measured $r_1$= 13510 ± 250 $mM^{-1}s^{-1}$ and $r_2$= 15815 ± 300 $mM^{-1}$ $s^{-1}$. The relaxivity values for GdDOTA-$SiO_2$@Au with Au cores of 5 nm are close to those obtained for GdDOTA-$SiO_2$@QD solution. In addition, a dramatic increase in relaxivity occurs if 10 nm Au nanoparticles are used instead of 5 nm Au cores. Together, this suggests that the surface area of the nanoparticle rather than the physical nature of the underlying core is the key factor for increased relaxivities.

To confirm the potentiality of our nanoprobe constructs, we perform preliminary dynamic contrast enhanced MR experiments in mice using a 1.5 T scanner. The nanoparticles were administered intravenously in the back of the mouse (100 µl, ~50 µM concentration in nanoparticles). Axial sections were collected at 8 seconds interval. Figure 6 represents two $T_1$-weighted images taken at the level of the bladder before the injection (left) and 5 minutes after the injection (right). The section of the animal is delineated by the thin white line in the left picture. The images have a similar contrast, except at the level of the bladder indicated by the arrow, where the signal increases with time; we attributed it to the clearance of the nanoparticles by the renal system. We observe accumulation of the nanoparticles as early as 300 s after injection.

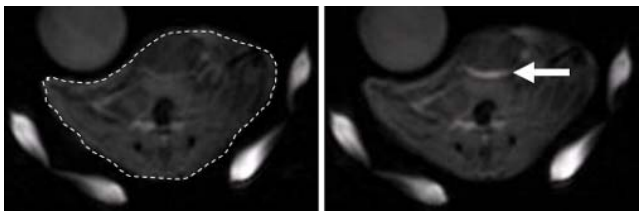

**Figure 6** Axial $T_1$ weighted image at the section of the bladder. The mouse body section is highlighted by the dashed white line in the left figure. Feature outside this line correspond to catheters and capillary tubes. The bladder is the pooch at the top-center of the mouse. Five minute after injection, nanoparticles start to accumulate in the bladder (right image, arrow). Notice how the contrast comes from only the lower part of the bladder, possibly indicating the sedimentation of the nanoparticles in the pooch.

From preliminary data, we observe an enhanced contrast in the bladder, possibly in the liver, and in what seems to be a major blood vein. No contrast enhancement is seen in the kidneys. It is worth noticing that the mice do not seem to suffer from the injection of the silica-coated nanoparticles, indicating a good tolerance to these foreign contrast agents.

## 4. Discussion

We have presented a paramagnetic nanoprobe of about 10-15 nm in diameter that consists in an inner inorganic particle protected with an ultra-thin silica shell to which several chelated paramagnetic ions are covalently linked. Before discussing the properties of such probes as MRI contrast agents and the advantages of using a silica shell in biomedical applications, we first comment on the synthetic route to grow an ultathin paramagnetic silica shell around nanocrystals of different nature.

**Growing a nm-thin silica shell around Au colloids and other cores:** The synthesis and use of semiconductor QDs coated with an ultra thin silica shell has been thoroughly described.[14, 15] In this paper we have extended the procedure to embed Au colloids of 5 nm and 10 nm diameter into a thin silica shell. The synthesis of silica shells around Au cores has been detailed in Liz-Marzan *et al.* pioneering work.[26] The authors used a 15 nm Au seed and showed how to grow thick shells (up to > 80 nm) over a period of several days.

Two main issues in growing a silica shell around Au seeds are the avoidance of cross-linking between nanoparticles and the control of the polymerization rate. The latter calls for the use of an anhydrous solvent, while the former calls for diluted solutions of nanparticles. This is because polycondensation of methoxysilane into siloxane bonds is driven by hydrolysis and heat/basicity. We want neither of these conditions. First, citrate-stabilized Au colloids are poorly soluble in solvents other than water (including aqueous buffers). Second we should dilute 20 ml of as-purchased 5 nm Au colloids (83 nM) in more than 500 mL of water to start with published protocols. The approach we develop here permits to silanize Au colloids in small volumes (<1-3 ml) at high nanoparticle concentration (> 1 μM for 5 nm Au). It is amenable to an easy scale-up and is applicable to the silanization of other inorganic cores such as iron oxide. [27]

Our silanization protocol for Au colloids calls for an exchange of the citrate capping ligands with a phosphine stabilizer (Bis(*p-sulfonatophenyl)phenylphosphine*), as described thoroughly in the literature. [16, 17] Phosphine-stabilized Au colloids are soluble in buffers and water at concentrations ~50-100–fold higher than the original ones; we silanize the nanoparticles at these high concentrations. The phosphine capping is just an intermediate step to allow manipulation of Au colloids in water and preventing their aggregation. To grow the silica shell, phosphine groups are replaced with thiolate primers, specifically mercaptopropyltrimethoxysilane or MPS. Because of the strong affinity between thiols and gold surfaces, the capping exchange is fast (<20 min) and efficient. The methoxysilane or silanol groups of MPS act as an anchor molecule upon which the silica shell forms. The consolidation and polymerization of MPS into a siloxane or silica shell can be controlled by choosing weakly alkaline aqueous solutions (pH~7.5-8) instead of heat. While the shell is slowly forming, fresh MPS and PEG-siloxane are incorporated into the shell. The shell growth is finally quenched by converting the remaining silanol groups into unreactive methyl groups. At this point silanized Au colloids can be purified from excess silane by dialysis, repeated runs in centricon 100 devices, and size-exclusion column.

The whole procedure for silanizing Au colloids takes about 3 hrs and is performed at particle concentration above ~ 1 μM for 5nm Au cores and above 0.1 μM for 10nm cores. We found that the same protocol works for both sizes of Au colloids. There is no evidence of aggregation of particles during the silanization process. The plasmon peaks of citrate-Au solutions and silanized-Au solutions are at the same wavelength (~524 nm *vs* ~526 nm respectively). The UV-Vis spectrum of silanized Au solutions is stable for weeks, even though silanized Au solutions are stored at high concentrations in a 10 mM phosphate buffer. Gel electrophoresis mobility of silanized Au is qualitatively similar to that of silanized QD nanoparticles.

**Paramagnetic silica shell as a generic scaffold for multivalent contrast agents:** The ability to grow silica shells around inorganic cores has several advantages: first the nanoparticles are extremely soluble in a wide variety of conditions (4<pH<11, and ionic strengths above 1M of phosphate buffer and 50 mM for buffers with divalent ions). Silanized nanoparticles are also stable in 1x PBS buffer at concentrations exceeding 50 μM. Although viscous at these concentrations, the solutions flow without resistance through capillaries used for the administration of the contrast agent in small animals. Second, the overall size of the nanoparticles remains small since the silica shell only adds a few nm to the particle diameter. We estimate that the silica shell around the 5 nm Au cores is only 2 nm thick. This results in particle size of about 9 nm. Similarly, we estimate that the silica shell adds about 2-4 nm to Au colloids of 10 nm in diameters, with a resulting total size of 15-18 nm. Finally, bioconjugation strategies to attach biomolecules to silica are well-developed. This is illustrated by the covalent linking of GdDOTA to the silanized nanoparticles. We link together the thiols of the silica shells with amines groups on the paramagnetic chelated species using the ubiquitous sulfo-SMCC (scheme 1). The linking protocol follows closely the one we develop to covalently bind DNA to silanized QD. [28, 29]

The design for this MRI contrast agent combines an outer paramagnetic shell with an inorganic core. It can generally be described as GdDOTA-$SiO_2$@Particle. The great interest in such design is the possibility to select a material as the core particle that provides a signature orthogonal to the one provided by the paramagnetic

GdDOTA-$SiO_2$ shell. For example, the core provides an optical component (fluorescence), while the chelated paramagnetic ions linked to the outer shell contribute to MRI relaxivity. The strength of the design consists in the fact that the paramagnetic silica shell does not interfere with optical properties of the inorganic cores. For instance, the position of the plasmon peak of GdDOTA-$SiO_2$@Au shifts by less than 2 nm compared to citrate-stabilized Au. Similarly, the UV-Vis absorption and fluorescence emission of GdDOTA-$SiO_2$@QD are virtually similar to those of TOPO-capped QD. Although detailed investigations of fluorescence properties have not been performed in detail, side-to-side comparison of QD and GdDOTA-$SiO_2$@QD excited with a hand-held UV lamp shows that both solutions have fluorescence properties (color and intensity) undistinguishable to the naked eye. This approach, where optical and MRI properties arise from physically separated and weakly interacting entities, present several advantages over other approaches devised to make multivalent probes. For instance, attempts to dope the shell of fluorescent core/shell CdSe/ZnS nanoparticles with Mn impurities produce multimodal nanoparticles with quenched fluorescence and a relatively weak magnetic contribution.

Achieving high relaxivities does not require the use of an inorganic core of a specific nature, because the MRI contrast power is carried only by the paramagnetic silica shell. In fact, it may be possible to optimize the design and reach even higher relaxivity values by other combinations of lanthanide ions, chelators and inorganic nanoparticles. Any inorganic core that can be embedded into silica can be used as seed for high relaxivity contrast agents. This includes CdSe/ZnS, CdTe, Au, Ag, and any oxide nanocrystals, such as very small superparamagnetic iron oxide nanoparticles. [27]

**Mechamisms responsible for relaxivity enhancement:** In this study, we found that GdDOTA-$SiO_2$@QD and GdDOTA-$SiO_2$@Au with a diameter of about 8-10 nm (5 nm cores + 2 nm silica shell) exhibit relaxivities in excess of $r_1$ ~1000-2000 $mM^{-1}s^{-1}$ and $r_2$ ~ 3000 $mM^{-1}s^{-1}$ and are detectable at ~100 nM concentrations. One obvious reason for this enhanced relaxivity is the number of GdDOTA molecules that decorate the silica surface. Chemical analysis indicates that about 45-50 GdDOTA are covering the silica surface of $SiO_2$@Au with 5 nm cores. More than 250-300 GdDOTA were measured around $SiO_2$@Au with 10 nm cores. As a result, relaxivities skyrocketed to ~16'000 $mM^{-1}s^{-1}$ and the detection limit plunged in the 10 nM range.

While the number of paramagnetic chelated ions is certainly the major factor in enhancing the total relaxivity, more subtle effects may also contribute to it. They manifest themselves by increasing the contribution of every individual GdDOTA to the total relaxivity. To see this, the total relaxivities of the samples is divided by the number of GdDOTA and converted into an ion relaxivity. This translates into $T_1$ and $T_2$ ion relaxivities at 60 MHz of ~ 23 $mM^{-1}s^{-1}$ and 54 $mM^{-1}s^{-1}$ for GdDOTA-$SiO_2$@P and only 3-5 $mM^{-1}$ $s^{-1}$ for unbound GdDOTA.

Increased ion relaxivities are expected when GdDOTA is constrained in its rotational motion. This is observed for macromolecular conjugates.[10] It has also been observed in a recent study where paramagnetic lipids were desorbed around a QD nanoparticle and relaxivities in the range of 2000 $mM^{-1}s^{-1}$ at 60 MHz were measured. [30] It was determined that about ~150 GdDOTA-lipids were surrounding the nanoparticle scaffold. Consequently, at 60 MHz, every Gd ion in the lipid payload was contributing by about 12 $mM^{-1}s^{-1}$ to the spin-lattice relaxivity $r_1$ and by about 18 $mM^{-1}s^{-1}$ to the spin-spin relaxivity $r_2$. It was mainly assumed that the increase in ion relaxivity came from the reduced tumbling rate of GdDOTA due to its covalent linking to a higher molecular weight macromolecule and the consequent increase in its rotational correlation time.

Our probes are quite similar to these, except that the paramagnetic lipid coat is replaced with a thinner paramagnetic silica shell. Yet, this change alone seems to affect the ion relaxivities. The values for the paramagnetic silica shell are 2 to 3 times higher than the values obtained with the paramagnetic lipid. As a result, our probes reach the same sensitivity with twice to three times less Gd(III) load. Although the rotational correlation time may be slightly different for these two systems, it is unlikely that it alone accounts for this large difference in relaxivity. We believe that a second reason for the increase in ion relaxivity comes from the very hydrophilic environment around GdDOTA provided by the silica shell. Silica is much more hydrophilic than lipids. It is likely that it generates a denser water solvation shell around the nanoparticle which forces more protons to interact with GdDOTA. We rule out that the high permanent electric dipole of the $SiO_2$@QD can affect the dynamic of water proton markedly, because the replacement of a QD core with a dipole-free Au particle of similar size produces a similar increase in ion relaxivity.

It is instructive to observe that ion relaxivities for GdDOTA-$SiO_2$@P are very close to those obtained for high generation organic dendrimer-GdDOTA ($N$>7) where ion relaxivities reach a plateau at 35 $mM^{-1}s^{-1}$ and 43 $mM^{-1}s^{-1}$ respectively.[31] In general, data for GdDOTA-$SiO_2$@P suggest that their MRI properties can be satisfactorily described within the framework of the classical relaxation theory.[10]

**Relaxivity of GdDOTA-$SiO_2$@nanoparticles *vs* other contrast agents**: Nanoparticles embedded into paramagnetic GdDOTA-$SiO_2$ shells reach relaxivities of a few thousands $mM^{-1}s^{-1}$ well in excess of the few, to a few tens $mM^{-1}s^{-1}$ observed for individual GdDOTA.[10] They surpass the relaxivity of hyperbranched dendrimers of

generation N=5. [32] In fact, their relaxivities are surpassed only by the relaxivity of highly complex and branched organic dendrimers of generations $N \geq 7$ [31] and iron oxide nanoparticles with core size above 20-40 nm.[6] Our probes compared favorably with the most promising new types of MRI contrast agent technology based on ultrasmall iron oxide nanoparticles. [33-35] For instance, a recent report indicated that Au-coated iron oxide nanoparticles with a size of 19 nm have ion relaxivities of only 3 $mM^{-1}s^{-1}$ in the 30-50 MHz range.[35] Considering that there are a few thousand Fe ions per nanoparticle, this translates into total relaxivities estimated in the ~10'000-20'000 $mM^{-1}s^{-1}$ range. At this size range however, the surface chemistry of iron and iron oxide is not yet well developed. Nanoparticles are often solubilized by ligand exchange,[33, 34] although such approach is unlikely to have widespread use *in vivo* because of the non-covalent nature of the passivating bonds. Cross-linked, stable and robust shells are necessary. Silica shells,[27] Au shells[35] and clustering into polymeric micelles[13] have been investigated. However, owing to the poor control of surface chemistry, extensive aggregation is often observed for several of these formulations making them unsuitable for *in vivo* imaging.

Our MRI probes exhibit a very high solubility and stability. They also represent a compromise between very high relaxivity values (> 100'000 $mM^{-1}s^{-1}$) obtained with large iron oxide particles (> 50-200 nm) and small "protein-like" sizes of branched dendrimers with relaxivities around 1000 $mM^{-1}s^{-1}$. [32] In addition, our MRI probes can be made in a few hours, in an Eppendorf tube using water as main solvent and a benchtop centrifuge for purification. The design has considerable potential for scale-up and plenty of room for tailoring the surface to specific biological applications (linking of targeting agent for instance).

**Advantages of a paramagnetic silica shell coating in biology**: Bare inorganic nanocrystals tend to aggregate in aqueous solutions and adsorb plasma or other proteins through non-specific interactions. To prevent their aggregation and tailor their surface properties, nanocrystals must be stabilized and embedded into a biocompatible and robust shell. Silica presents several advantages over polymer-based shells. Unlike polymers, silica is not subjected to microbial or macrophage attack and it neither swells nor changes shape and porosity with changing pHs. Silica is chemically inert and therefore does not influence the redox reaction of the core surface. Furthermore, the chemistry to functionalize silica is well-developed. It is straightforward to introduce thiols, amine or carboxylic groups onto a silica surface. The groups can be further derivatized with targeting biomolecules using established bioconjugation techniques. [20] Finally, it is much easier to control the polymerization of siloxane into silica (and hence the size of the silica shell) than it is to control the thickness of a polymer-based coating. For example, FCS and dynamic light scattering measurements indicated that while silica-coated 5 nm Qdots have a hydrodynamic radius of 9-11 nm, polymer-embedded 5 nm Qdots have a hydrodynamic radius close to 30 nm [36] and 19 nm Au-coated iron oxide close to ~250 nm. [35]

Silica has other advantages over polymeric nanoparticles that have emerged in recent live cell studies: low toxicity. Silica-coated nanoparticles exhibit much smaller cytotoxicity than polymer-coated nanoparticles.[37] Even more remarkable, silica-coated nanoparticles were shown to have negligible perturbation on the gene expression patterns of lung and skin epithelials cells. [38] This suggests that silica-coated nanoparticles pose minimal interference with the normal physiology and metabolism of these cells lines. Because silica-coated nanoparticles can be functionalized with a wide array of targeting biomolecules, [15, 28, 29] they can be biologically programmed to recognized critical phosphorylation sites, proteases and nucleases, motor proteins, or surface receptors on organelles such as the cell nucleus. [39] These nanoparticles may play a key role in cell biology for deciphering molecular pathways. Toxicity studies at the gene expression level of silica-coated nanoparticles on other cells lines, tissues or animal models has not been investigated so far and are undoubtably an emerging research area.

**Preliminary in vivo assays – successes and pitfalls**

In a series of early *in vivo* assays, the contrast agent based on paramagnetic silanized nanaoparticles was injected into live mice. We injected about $6x10^{15}$ particles (i.e. ~200 μl at 50 μM) and did not observe adverse effects on the health of the animals. In fact, the vast majority of silanized particles are excreted into the bladder. In dynamics contrast enhanced studies, we observe the accumulation of the nanoprobes in the bladder within minutes of the injection. We do not observe a contrast enhancement from other organs, indicating that the large majority of the nanoprobes are filtered out by the renal system.

The fact that silanized nanoparticles are not taken up by the different organs in a significant manner is a positive sign, in particular in view of the fears of potential toxicity of the nanomaterials. In contrast, low retention time is the bloodstream represents a potential pitfall many applications including for angiogenesis, i.e. the formation of new blood vessels. However, both specific uptake and retention time can be implemented or improved by tailoring the surface chemistry of nanoparticles, for instance by grafting targeting peptides or longer PEG chains.

At this stage, it is still an open question whether paramagnetic silica nanoparticles will have the ability to transverse the extracellular matrix surrounding blood vessels and microvsculatures, and if they will have the ability to recognize cancer cells and delineate the contours of a tumor. It is likely that both size and surface

composition will play key roles for such endeavors. The discussion above highlights the need of a tailored surface chemistry, but neglect to mention the importance of the "size" parameter. Indeed, if the probes are too big, they will have a reduced ability to diffuse in tumoral microvasculature and transverse the extracellular matrix, as they have a limited ability to cross cellular membranes. Although the ideal size of a probe is not known, we hypothesize that probes with sizes in the 10-20 nm range, as the ones we developed and with an appropriate surface chemistry, represent the best candidates since they mimic the size of therapeutic antibodies.

In order to use our silica-coated nanoparticles for angiogenesis or other targeted applications (stem cell tracking, where a small number of parent cells can be labeled, implanted and their progeny followed *in vivo*, [33] guided surgery, …), the total relaxivity and contrast power of our probes will have to be enhanced even further. An in-depth comparison with conventional contrast agents (Magnevist, Dotarem, …) is underway. We estimate that we need to increase the number of GdDOTA from ~50 to ~500 in the Qdots probes, to have sufficient contrast enhancement for in vivo applications. This challenge seems feasible.

## 4. Conclusions

We have described a strategy to embed inorganic nanoprobes into a paramagnetic silica shell. The shell is rendered paramagnetic by covalently linking GdDOTA to its surface. Once attached to the surface, each of these contrast agent units exhibit $T_1$ and $T_2$ ion relaxivities at clinical fields that are respectively 9 and 18 times larger than the ion relaxivities of unbound GdDOTA. We provide evidence that the increase is not related to the nature of the inorganic core but most likely to the fact that GdDOTA are bound to a hydrophilic silica surface which reduces their rotational motion.

What matters for imaging purposes is not primarily the ion relaxivity of a contrast agent, but its total relaxivity. Similar to the case of dendrimeric polymers, multiple GdDOTA can be anchored onto the surface of a single silica nanoparticle. Since the ion relaxivity is additive, we have measured $T_1$ and $T_2$ relaxivitites at room temperatures and at clinical fileds in the order of 1000-3000 $mM^{-1}$ $s^{-1}$ for GdDOTA-$SiO_2$@Particle with particle cores of 5 nm, resulting from the contribution of ~ 50 GdDOTA. If the particle cores are 10 nm, the surface area of silica shells permits the linking of ~250-300 GdDOTA. Remarkably, these latter probes exhibit relaxivities in excess of 15000 $mM^{-1}s^{-1}$ at room temperature and clinical fields.

The paramagnetic silica shell has been grown around semiconductor and metallic nanoparticles. There are however no restriction in the use of the core material. It may be envisioned to grow a GdDOTA-$SiO_2$ around a (superpara)magnetic core such as small SPIO $Fe_3O_4$ or $Fe_2O_3$. In that configuration, perturbation in the dynamic response of water protons will come from the presence of the paramagnetic GdDOTA-$SiO_2$ shell and from the inner SPIO cores. We expect such systems to present even higher relaxivities values that the ones obtained here.

Preliminary in vivo tests indicate that paramagnetic silica-coated nanoparticles provide a contrast enhancement in MRI, as evidenced by the signal coming from their accumulation in the bladder. However, higher sensitivities will be needed to obtain valuable information in MRI on a peculiar biological issue.

The design of our probe allows its straightforward conversion into a PET probe. For that, only a handful of DOTA have to be loaded with a radioisotope (i.e. $^{64}Cu$) instead of Gd(III). The overall probe will maintain a unique surface chemistry. However since PET sensitivity far exceeds MRI sensitivity, it is possible to test basic properties of the probes, such as their potential leakage from the vascular system, their non-specific uptake by different organs, or their ability to recognize tumors. These studies, currently underway, will provide powerful complementary information on the compatibility and utility of inorganic nanoprobes for *in vivo* imaging.

**Acknowledgements**

We would like to thank Giulia Galli and Natalia Zaitseva for their support. This work was performed under the auspices of the U.S. Dept. of Energy at the University of California/Lawrence Livermore National Laboratory under contract no. W-7405-Eng-48.

**References**

1. Tsien, R. Y., Imagining imaging's future. *Nature Cell Biology* **2003**, SS16-SS21.
2. Alivisatos, A. P.; Gu, W.; Larabell, C., Quantum Dots as Cellular Probes. *Annu Rev Biomed Eng* **2004**.
3. Dahan, M., Watching the dynamics of individual proteins in live cells using quantum dots. *Journal of Histochemistry & Cytochemistry* **2004,** 52, S18-S18.
4. Courty, S.; Luccardini, C.; Bellaiche, Y.; Cappello, G.; Dahan, M., Tracking Individual Kinesin Motors in Living Cells Using Single Quantum-Dot Imaging. *Nano Lett.* **2006,** 6, (7), 1491 -1495.
5. Bremer, C.; Weissleder, R., Molecular imaging - In vivo imaging of gene expression: MR and optical technologies. *Academic Radiology* **2001,** 8, (1), 15-23.
6. Gimi, B.; Pathak, A. P.; Ackerstaff, E.; Glunde, K. A., D.; Bhujwalla, Z. M., Molecular imaging of cancer: applications of magnetic resonance methods. *Proceedings of the IEEE* **2005,** 93, (4), 784-799.
7. Weissleder, R., A clearer vision for in vivo imaging. *Nature Biotechnology* **2001,** 19, (4), 316-317.

8. Weissleder, R., Scaling down imaging: Molecular mapping of cancer in mice. *Nature Reviews Cancer* **2002,** 2, (1), 11-18.
9. Allport, J. R.; Weissleder, R., In vivo imaging of gene and cell therapies. *Experimental Hematology* **2001,** 29, (11), 1237-1246.
10. Caravan, P.; Ellison, J. J.; McMurry, T. J.; Lauffer, R. B., Gadolinium(III) chelates as MRI contrast agents: Structure, dynamics, and applications. *Chemical Reviews* **1999,** 99, (9), 2293-2352.
11. Jacques, V.; Desreux, J. F., New Classes of MRI Contrast Agents. *Topics in Current Chemistry* **2002,** 221, 123-164.
12. Thompson, M. K.; Botta, M.; Nicolle, G.; Helm, L.; Aime, S.; Merbach, A. E.; Raymond, K. N., A highly stable Gadolinium complex with fast, associative mechanism of water exchange. *J. Am. Chem. Soc.* **2003,** 125, 14274-14275.
13. H. Ai; Flask, C.; Weinberg, B., X. T. S. M.; Pagel, D.; Farrell, D.; Duerk, J.; Gao, J., Magnetite-Loaded Polymeric Micelles as Ultrasensitive Magnetic-Resonance Probes. *Advanced Materials* **2005,** 17, (16), 1949-1952.
14. Gerion, D.; Pinaud, F.; Williams, S. C.; Parak, W. J.; Zanchet, D.; Weiss, S.; Alivisatos, A. P., Synthesis and properties of biocompatible water-soluble silica- coated CdSe/ZnS semiconductor quantum dots. *Journal of Physical Chemistry B* **2001,** 105, (37), 8861-8871.
15. Wolcott, A.; Gerion, D.; Visconte, M.; Sun, J.; Schwartzberg, A.; Chen, S.; Zhang, J. Z., Silica-coated CdTe quantum dots functionalized with thiols for bioconjugation to IgG Proteins. *J. Phys. Chem. B* **2006,** 110, 5779-5789.
16. Zanchet, D.; Micheel, C. M.; Parak, W. J.; Gerion, D.; Alivisatos, A. P., Electrophoretic isolation of discrete Au nanocrystal/DNA conjugates. *Nano Lett.* **2001,** 1, 32-35.
17. Loweth, C. J.; Caldwell, W. B.; Peng, X.; Alivisatos, A. P.; Schultz, P. G., DNA-Based Assembly of Gold Nanocrystals. *Angewandte Chemie International Edition* **1999,** 38, (12), 1808-1812.
18. Wang, X. Y.; Jin, T. Z.; Comblin, V.; Lopezmut, A.; Merciny, E.; Desreux, J. F., A Kinetic Investigation of the Lanthanide Dota Chelates - Stability and Rates of Formation and of Dissociation of a Macrocyclic Gadolinium(Iii) Polyaza Polycarboxylic Mri Contrast Agent. *Inorganic Chemistry* **1992,** 31, (6), 1095-1099.
19. Prantner, A. M.; Sharma, V.; Garbow, J. R.; Piwnica-Worms, D., Synthesis and characterization of a Gd-DOTA-D-permeation peptide for magnetic resonance relaxation enhancement of intracellular targets. *Molecular Imaging* **2003,** 2, (4), 333-341.
20. Hermanson, G. T., *Bioconjugate techniques*. Academic Press, Inc.: San Diego, CA, 1996.
21. Yu, W. W.; Qu, L. H.; Guo, W. Z.; Peng, X. G., Experimental determination of the extinction coefficient of CdTe, CdSe, and CdS nanocrystals. *Chemistry of Materials* **2003,** 15, (14), 2854-2860.
22. Lauffer, R. B., Paramagnetic Metal-Complexes as Water Proton Relaxation Agents for Nmr Imaging - Theory and Design. *Chemical Reviews* **1987,** 87, (5), 901-927.
23. Aime, S.; Botta, M.; Fasano, M.; Geninatti Crich, S.; Terreno, E., 1H and 17O-NMR relaxometric investigations of paramagentic contrast agents for MRI. Clues for higher relaxivities. *Coordination Chemistry Reviews* **1999,** 185-186, 321-333.
24. Aime, S.; Cabella, C.; Colombatto, S.; Crich, S. G.; Gianolio, E.; Maggioni, F., Insights into the use of paramagnetic Gd(III) complexes in MR-molecular imaging investigations. *Journal of Magnetic Resonance Imaging* **2002,** 16, (4), 394-406.
25. Li, L.-s.; Alivisatos, A. P., Origin and Scaling of the Permanent Dipole Moment in CdSe Nanorods. *Physical Review Letters* **2003,** 90, (9), 097402.
26. Liz-Marzan, L. M.; Giersig, M.; Mulvaney, P., Synthesis of Nanosized Gold-Silica Core-Shell Particles. *Langmuir* **1996,** 12, (18), 4329-4335.
27. He, Y. P.; Wang, S. Q.; Li, C. R.; Miao, Y. M.; Wu, Z. Y.; Zou, B. S., Synthesis and characterization of functionalized silica-coated Fe3O4 superparamagnetic nanocrystals for biological applications. *J. Phys. D: Appl. Phys.* **2005,** 38, 1342-1350.
28. Gerion, D.; Parak, W. J.; Williams, S. C.; Zanchet, D.; Micheel, C. M.; Alivisatos, A. P., Sorting fluorescent nanocrystals with DNA. *Journal of the American Chemical Society* **2002,** 124, (24), 7070-7074.
29. Gerion, D.; Parak, W. J.; Zanchet, D.; Woerz, A. S.; Pellegrino, T.; Micheel, C. M.; Williams, S. C.; Seitz, M.; Bruehl, R. E.; Bryant, Z.; Bustamante, C.; Bertozzi, C. R.; Alivisatos, A. P., Conjugation of DNA to silanized colloidal semiconductor nanocrystalline quantum dots. *Chemistry of Materials* **2002,** 14, (5), 2113-2119.
30. Mulder, W. J. M.; Koole, R.; Brandwijk, R. J.; Storm, G.; Chin, P. T. K.; Strijkers, G. J.; deMelloDonega, C.; Nicolay, K.; Griffioen, A. W., Quantum Dots with a Paramagnetic Coating as a Bimodal Molecular Imaging Probe. *Nano Lett.* **2006,** 6, (1), 1-6.
31. Bryant Jr, L. H.; Brechbiel, M. W.; Wu, C.; Bulte, J. W. M.; Herynek, V.; Frank, J. A., Synthesis and relaxometry of high-generation (G = 5, 7, 9, and 10) PAMAM dendrimer-DOTA-gadolinium chelates. *Journal of Magnetic Resonance Imaging* **1999,** 9, (2), 348-352.
32. Langereis, S.; de Lussanet, Q. G.; van Genderen, M. H. P.; Meijer, E. W.; Beets-Tan, R., G.H.; Griffioen, A. W.; van Engelshoven, J. M. A.; Backes, W. H., Evaluation of Gd(III)-DTPA-terminated poly(propylene imine) dendrimers as contrast agents for MR imaging. *NMR Biomed* **2006,** 19, 133-141.
33. Song, H.-T.; Choi, J.-s.; Huh, Y.-M.; Kim, S.; Jun, Y.-w.; Suh, J.-S.; Cheon, J., Surface Modulation of Magnetic Nanocrystals in the Development of Highly Efficient Magnetic Resonance Probes for Intracellular Labeling. *J. Am. Chem. Soc.,* **2005,** 127, (28), 9992 - 9993.
34. Jun, Y.-w.; Huh, Y.-M.; Choi, J.-s.; Lee, J.-H.; Song, H.-T.; Kim, S.; Yoon, S.; Kim, K.-S.; Shin, J.-S.; Suh, J.-S.; Cheon, J., Nanoscale Size Effect of Magnetic Nanocrystals and Their Utilization for Cancer Diagnosis via Magnetic Resonance Imaging. *J. Am. Chem. Soc.* **2005,** 127, (16), 5732 -5733.
35. Cho, S.-J.; Jarrett, B. R.; Louie, A. Y.; Kauzlarich, S. M., Gold-coated iron nanoparticles: a novel magnetic resonance agent for T1 and T2 weighted imaging. *Nanotechnology* **2006,** 17, 640-644.
36. Doose, S.; Tsay, J. M.; Pinaud, F.; Weiss, S., Comparison of Photophysical and Colloidal Properties of Biocompatible Semiconductor Nanocrystals Using Fluorescence Correlation Spectroscopy. *Anal. Chem.* **2005,** 77, (7), 2235 -2242.
37. Kirchner, C.; Liedl, T.; Kudera, S.; Pellegrino, T.; Muñoz Javier, A.; Gaub, H. E.; Stölzle, S.; Fertig, N.; Parak, W. J., Cytotoxicity of Colloidal CdSe and CdSe/ZnS Nanoparticles. *Nano Letters* **2005,** 5, (2), 331-338.
38. Zhang, T.; Gerion, D.; Stilwell, J.; Ding, L.; Elboudwarej, O.; Cooke, P. A.; Alivisatos, A. P.; Gray, J. W.; Chen, F., Cellular Effect of high doses of silica-coated Qdots profiled with high-throughput gene expression analysis and high content cellomics measurements. *Nano Lett.* **2006,** 6, (4), 800-808.
39. Chen, F.; Gerion, D., Fluorescent CdSe/ZnS nanocrystal-peptide conjugates for long-term, nontoxic imaging and nuclear targeting in living cells. *Nano Letters* **2004,** 4, (10), 1827-1832.